# Modelling of tungsten contamination and screening in WEST plasma discharges

S. Di Genova, A. Gallo, N. Fedorczak, H. Yang, G. Ciraolo, J. Romazanov, Y. Marandet, H. Bufferand, C. Guillemaut, J.P. P Gunn, et al.

# Modelling of tungsten contamination and screening in WEST plasma discharges

S. Di Genova [1], A. Gallo[2], N. Fedorczak[2], H. Yang[2], G. Ciraolo[2], J. Romazanov[3], Y. Marandet[4], H. Bufferand[2], C. Guillemaut[2], J. P. Gunn[2], C. Gil[2], E. Serre[1], S. Brezinsek[3] and the WEST team[5]

[1]M2P2, Aix-Marseille Univ, CNRS, Centrale Marseille, 13013 Marseille, France
[2]IRFM, CEA-Cadarache, 13108 Saint-Paul-lez-Durance, France
[3]IEK-4, Forschungszentrum Jülich, 52425 Jülich , Germany
[4]PIIM, Aix-Marseille Univ, CNRS, 13013 Marseille, France
[5]http://irfm.cea.fr/en/west/WESTteam/

**Abstract**

The WEST experiment is currently operating with tungsten plasma-facing components and testing ITER-like divertor monoblocks. In order to support WEST experiments interpretation, numerical analyses were carried out. Starting from WEST experimental data, realistic background plasma conditions were reproduced through SolEdge-EIRENE and used as input for ERO2.0 simulations to investigate tungsten migration. Tungsten contamination due to the different plasma-facing components was modelled under different plasma conditions, highlighting a non-negligible contribution of tungsten coming from the tokamak main chamber. Tungsten penetration factor was computed and used as an indication for tungsten screening by the background plasma at the different tokamak plasma-facing components. Simulations showed the main chamber components to be very weakly screened. Light impurities charge was showed to influence not only tungsten sputtering, but also its probability to enter the confined plasma. Simulations results indicated that even when the tungsten source is not heavily influenced by self-sputtering, contamination of the confined plasma can be strongly impacted by it in low density

background plasma conditions. Finally, a one-to-one comparison between tungsten visible spectroscopy at the lower divertor from experimental data and from synthetic diagnostics was performed, showing that it is possible to reproduce a realistic lower divertor signal following experimental evidence on light impurities asymmetry between the targets.

# 1 Introduction

Tungsten (W) is one of the most suitable materials for the inner wall of magnetic confinment fusion devices due to its very high heat conductivity, high melting point, low fuel retention, and low sputtering yield. Nevertheless, even small quantities of partially ionised W ions entering in the confined plasma as impurities can trigger very high power losses through radiation and hence a reduction of central plasma temperature and, consequently, of the fusion reaction rate. For this reason, in view of future fusion reactors, we need to study W impurities source and transport starting from currently operating machines through both experiments and modeling.
The ITER divertor will also be made of bulk W monoblocks [1]: these plasma-facing components (PFCs) are at present being tested in the W Environment Steady-state Tokamak (WEST) [2]. This machine is equipped with PFCs made of bulk W or W-coated CFC and presents strong core radiation losses most probably due to W contamination. At present, only the gross W erosion is experimentally estimated in WEST [3,4] whereas no experimental estimate of the net W erosion is available. Therefore, modeling efforts are required to study W prompt redeposition and net erosion as well as to identify which PFCs are responsible for the highest contamination of the confined plasma.
In this work we used numerical modelling to study W net sources and transport mechanisms in WEST L-mode discharges: starting from experimental data we modelled the background plasma with 2D transport simulations using the SolEdge-EIRENE package [5] and we subsequently performed 3D Monte Carlo (MC) simulations to study W contamination with the ERO2.0 code [6]. Similar approaches were adopted for several wall materials using different numerical models: OEDGE- ERO2.0 for berylium in ITER [7], EMC3-EIRENE for carbon in LHD [8], and SOLPS-ITER-IMPGYRO for W in ITER [9].
H-mode discharges were not modelled in this work. Nevertheless, it has to be remarked that the presence of edge localised modes during H-mode can have a vital impact on machines equipped with W PFCs [10].
The paper is organized as follows: in section 2 a representative WEST plasma

discharge and the corresponding plasma simulations are presented; in section 3 the set-up of the MC simulations tracking W impurities is described; in section 4 the role of the different PFCs in WEST W contamination from the simulations is discussed followed by an analysis of the influence of light impurities on the capability of heavy wall impurities to reach the separatrix in section 5; in section 6 the role of self-sputtering in plasma contamination in different plasma conditions is discussed; finally, in section 7 a direct comparison with experimental data of the WI emission line from visible spectroscopy is carried out.

# 2 Modelling of the WEST background plasma

The numerical studies on W contamination performed in this work were based on the modelling of the WEST plasma discharge #55797 (figure 1). This is a typical WEST plasma discharge without external seeding of impurities. When the current flat-top phase is reached, the injected power is around 1 MW (3.4 s). Subsequently, external heating through LH antennae is injected amounting to about 5 MW in the flat-top phase (5.5 s) with the central line integrated density (CLID) achieving $4.5\times10^{19}$ m$^{-2}$. Modelling was performed on two different phases of the discharge: the first one is in the interval of time $3-3.5$ s, at the end of the Ohmic phase, and the second one in the interval of time $5-5.5$ s, during the end of the external heating ramp-up.
In figure 1b the magnetic flux coordinate $\psi_N$ iso-surfaces of the magnetic reconstruction [11] are shown. $\psi_N$ is defined as $\psi_{\mathrm{N}} = (\psi - \psi_{\mathrm{ax}})/(\psi_{\mathrm{sep}} - \psi_{\mathrm{ax}})$, where $\psi$ is the magnetic flux, $\psi_{\mathrm{ax}}$ is the magnetic flux at the magnetic axis, and $\psi_{\mathrm{sep}}$ is the magnetic flux at the separatrix. Poloidal positions of WEST main PFCs are also shown in the figure.

The simulations of the plasma during the two phases were performed using the code package SolEdge-EIRENE. The package consists in a coupling between the multi-fluid code SolEdge [5] and the MC neutral solver EIRENE [12]. For this work we used the latest SolEdge version, named SolEdge3X [13–15]. At the time of writing, the modelling of complex non-axisymmetric 3D limiters in SolEdge required further development. Hence, the SolEdge-EIRENE simulations presented in this work were performed in 2D mode assuming an axisymmetric wall. This idealisation strongly overestimates the antenna limiter surface wetted by the plasma in the machine. For this reason, the axisymmetric antenna in the simulation was positioned further away from the plasma compared to its actual position during the experiment, in order to lower the plasma flux at this component surface. Further considerations about the effects of an axisymmetric antenna on W

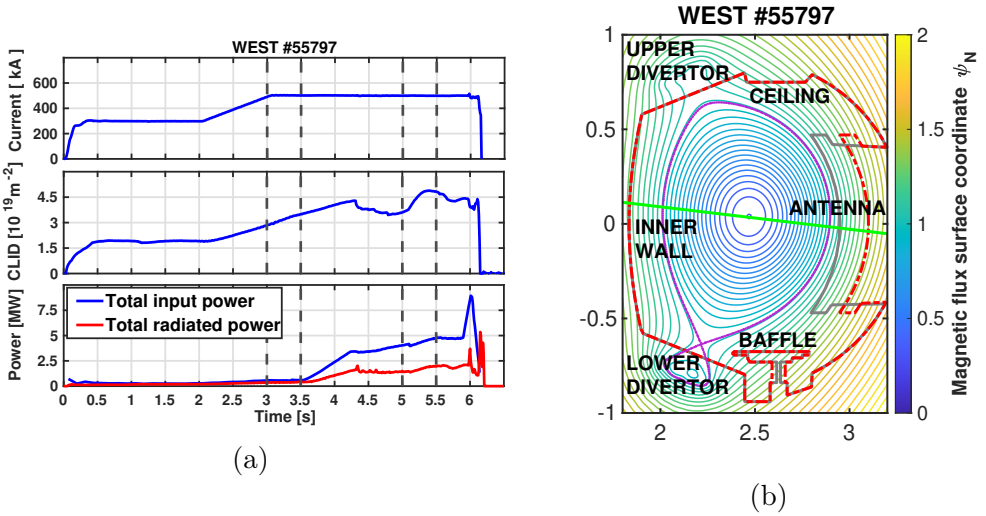


(a) (b)

Figure 1: a) Time trace of input and radiated power, central line integrated density (CLID), and plasma current in WEST discharge #55797. b) Magnetic flux coordinate $\psi_{\mathrm{N}}$ following the magnetic reconstruction of the discharge (produced with NICE [11]), central line of sight used for measure CLID (green line), and wall adopted in the SolEdge-EIRENE simulations (red dashed line), purple line indicates the separatrix.

erosion and migration in the model are presented in section 4. The wall geometry adopted in the simulations is shown in figure 1b (red dashed line).
The 2D simulations were performed assuming Deuterium (D) plasma since there was no seeding of external impurties in the discharge. The intrinsic content of light impurities in the tokamak was preferred to be added later in ERO2.0 simualtions as a free parameter to study its effect W sputtering and deposition (see sections from 4 to 7).
The net power crossing the separatrix $P_{\mathrm{SOL}}$ was considered to be lower than the actual one registered in the experiment to account for the radiation in the scrape-off layer (SOL) due to light impurities, so the adopted values were $P_{\mathrm{SOL}} = 0.45$ MW for the Ohmic phase and $P_{\mathrm{SOL}} = 2.50$ MW for the external heating phase, respectively.
The gas puff was located at the outer midplane (OMP) and was adjusted to obtain a peak value of electron temperature $T_{\mathrm{e}}$ comparable to the experimental one estimated by Langmuir probes embedded in the lower outer divertor target [16, 17]. The simulations were performed without self-consistent turbulence modelling, in the so-called transport mode. Hence, transport coefficients were adopted as a proxy for turbulent transport in the perpendicular direction. The transport coefficient for particles and momentum were cho-

sen to be equal to the experimentally estimated average anomalous diffusion value in WEST L-mode discharges $D = \nu = 0.3$ m$^2$/s, while the energy ones for ions and electrons were set to the standard value $\chi_i = \chi_e = 1$ m$^2$/s [18]. A uniform recycling coefficient R = 0.99 was adopted on the wall contour for modelling WEST W tiles, while the pump albedo coefficient was set to be $R_{pump} = 0.95$ (typical assumption for WEST pumping system). Drifts were switched off.
The plasma density during the two considered phases differ substantially in the SOL, with a factor of roughly 4 between them at the targets peak values, and also at the OMP separatrix so they will be referred to as "low" and "high" density plasma simulation in the following. The experimental data will be anyway shown with their acquisition time.
Comparison between SolEdge-EIRENE simulations and the lower divertor Langmuir probes are shown in figure 2, exhibiting a good match between probes and simulations at the divertor targets. It is possible to notice how, having adjusted the gas puff on the outer target peak $T_e$, electron density $n_e$ values at the targets are also reasonably recovered. While simulations are converged with respect to outer divertor target $T_e$, consistency of midplane profiles had to be verified. Edge density profile could be reconstructed from interferometry [19] inversion and sweeping reflectometry [20]. Note that interferometry inversion is subject to large uncertainties at the plasma edge due to weak constrains on the steep local gradients.
Plots of $n_e$ at OMP and comparisons with experimental interferometry are presented in figure 3, showing a qualitative agreement. For the first time interval of 3-3.5 s also the reflectometry data are reported, it is possible to see how simulations are closer to them than to the interferometry data. It has to be remarked that in simulations the plasma particle flux at the upper divertor is not negligible with respect to the lower divertor, with just a factor of 7 between the peak values. This is not consistent with what is usually seen in WEST experiments in lower single null magnetic configurations, where there is usually a factor of 10-100 between the divertors particle flux peak values. It is in principle possible to improve the reconstruction by an ad-hoc modification using experimental data [21] and this approach should be considered for future work, but this empirical correction is not always possible and was not repeated for this work.

The fluid simulations were used as fixed steady state background for ERO2.0 simulations (see sections 3-7). For this reason the SolEdge-EIRENE simulations will be referred to as background plasmas in the following.

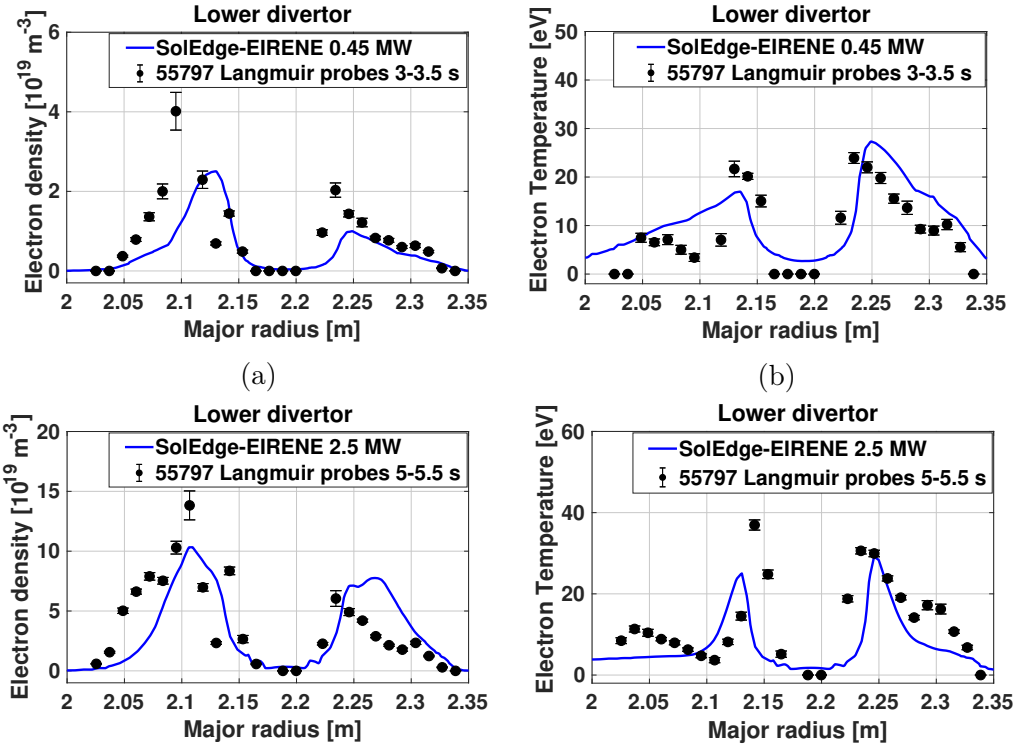


Figure 2: Comparison between simulations and Langmuir probes during $t = 3 - 3.5$ s (a and b), and during $t = 5 - 5.5$ s (c and d).

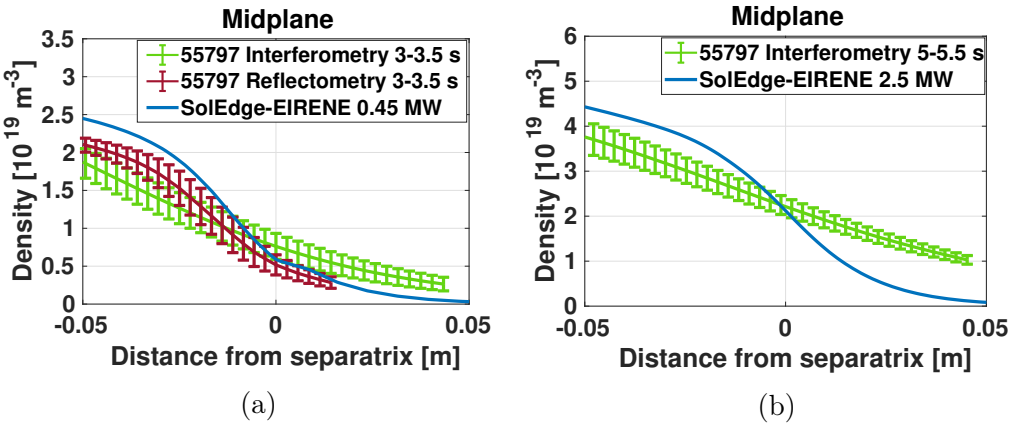


Figure 3: Comparison between simulations and interferometry during $t = 3 - 3.5$ s (a), and during $t = 5 - 5.5$ s (b).

# 3 Wall impurities erosion and transport simulations set-up

To estimate W re-deposition a kinetic description is needed. Also, the high number of possible W ionisation states makes it very demanding to study W transport with a multi-fluid code. For these reasons, a MC impurity tracker was more suitable for this study. ERO2.0 was the code adopted for the numerical modelling of W erosion and 3D transport across plasma [6, 22]. SolEdge-EIRENE simulations were used as input to obtain fluid background plasma for ERO2.0. The SolEdge EIRENE results data provided to ERO2.0 as input were spatial distributions of $n_{\mathrm{e}}$ (considered to be equal to the ion density), $T_{\mathrm{e}}$, the main ion temperature $T_{\mathrm{i}}$, the main ion parallel velocity $v_{\parallel}$, and the magnetic field $\vec{B}$. Uniform values of concentration were used for each light impurity ionisation state. Even if ERO2.0 is a 3D code, the wall geometry is fixed here by the background plasma through an axial revolution of the 2D poloidal section used in SolEdge-EIRENE simulations and so the antenna-limiter is considered to be an axysimmetric object, rather than a set of discrete toroidal distributed antennae as in the experiment. This has some important implications, as will be discussed in section 4.
Oxygen (O) was used as a proxy for the light impurities present in WEST (O, carbon, boron, nitrogen and others), and it was considered to be part of the background plasma inside the ERO2.0 simulations. Its global concentration was generally set to be 3% of the background plasma ions density (reasonable average value in WEST from experimental observations [4]), excluding special cases in which lower values were chosen to study the influence on the simulation of the parameter itself or in the case in which it was needed to compare results with experimental data, as it will specified in the text.
It is worth it to remark that considering different light impurities as a proxy would not in general change the conclusions of this work. The presence of light impurities in the plasma influences both W erosion and transport in tokamaks. In ERO2.0 simulations W sputtering is influenced by the presence of light impurities in the background plasma through the energy of the projectile ions impacting the wall, considered to be equal to $E_{\mathrm{i}} = 2T_{\mathrm{i}} + 3ZT_{\mathrm{e}}$, with temperature in eV (no convolutive effects of the Maxwellian energy distribution on the plasma interaction with a W wall are accounted by the code). This hypothesis may be not accurate if light impurities Mach number goes beyond unity under the effect of the friction with main ion plasma flowing at its own sound speed [23]. However, this assumption remains a common standard in absence of a more precise modelling of light impurities behaviour in the sheath [24], and the effect of light impurities impacting the wall at speeds

similar to the main ion sound speed might be discussed elsewhere.
The sputtering threshold energy depends on the mass ratio between the projectile ion and the target wall atom [24]. In WEST L-mode plasma discharge conditions described here, $T_e$ and $T_i$ are low enough to neglect W sputtering caused by D. On the other hand, the mass ratio between O (or carbon, or nitrogen) and W is high enough to make the light impurities sputtering completely dominate over the main ion sputtering.
W transport processes in ERO2.0 are computed following the Fokker-Planck model. In this model, the two collisional operators (friction and diffusion in the velocity space) are both influenced by the light impurities presence. Under the hypothesis introduced by ERO2.0, light impurities influence the collisional operators quadratically with the background effective charge $Z_{\text{eff}}$ and through the background plasma effective mass $m_{\text{eff}}$ (key parameter for the background plasma Maxwellian distribution).
High ionisation states of light impurities strongly influence the heavy impurities erosion. Moreover, they affect also their collisions across the plasma. However, if light impurities concentration is sufficiently low, the influence of light impurities on the collisional operators of the Fokker-Planck model is narrower than than the effect on the W sputtering yield.
For example, passing from a background plasma with 1% of $O^{1+}$ to one with 3% of $O^{3+}$, $Z_{\text{eff}}$ will pass from 1 to 1.1 , and $m_{\text{eff}}$ will pass from 2.10 amu to 2.42 amu. On the other hand, the O incident energy $E_i$ will pass from $2T_i + 3T_e$ to $2T_i + 9T_e$. Considering $T_e = T_i = 20$ eV and an incidence angle with the wall equal to 60°, the sputtering yield would pass from $1.2 \times 10^{-4}$ to $4.9 \times 10^{-3}$. From the previous example it is possible to understand how W sputtering is very sensible to the light impurities content. Hence, the uniform concentration of O ionisation state was set in order to model better the SOL region where the plasma-wall interaction occurs than the confined region inside the separatrix. Previously published multi-ion runs of SolEdge-EIRENE [21] suggest that not only the the lowest ionisation states are present in the SOL, but even a small amount of the highest ones. For simplicity, the only O ionisation states taken into account in the simulations are $O^+$, $O^{2+}$, and $O^{3+}$, assuming a concentration ratio with the total O concentration (sum over all the ionisation states) of 75 : 100, 15 : 100, and 10 : 100 respectively (except the case in which it will be explicitly differently reported). These assumptions are based on the fact that, at the wall, light impurties lower ionisation states are expected to be found in higher content, since they are ejected by the wall as neutrals.

The sampling of the particles sputtering position, i.e. the probability of the particles to start their trajectory at a certain point of the wall, was cho-

sen for this work to be equal to the normalized W gross erosion flux at the wall, while for the starting velocity distribution we adopted the Thompson distribution $dY \propto E(E+E_{\mathrm{b}})^{-\alpha}dE$ for the sputtering energy (where $Y$ is the sputtering yield, $E$ is the energy of the sputtered particle, $E_{\mathrm{b}}$ is the bond energy of wall particles and $\alpha$ was set to be the standard value 3), while we adopted a simple cosine distribution for the polar angle, considering the direction normal to the wall surface coincident with the 0 angle direction. Finally, uniform distribution for the azimuthal angle was adopted in simulations. Actually, more accurate distributions for the polar angle [25] and for the azimuthal one [26] are present in literature. However, common choices were prefered to make the simulations results interpretation simpler. For the sputtering yield, SDTrimSP5.0 simulations data were used [27].
No explicit terms for thermal forces were used in the Fokker-Planck model. Nevertheless, the collisional operators used in the simulations have a dependece on $T_{\mathrm{i}}$. Hence, temperature gradients had anyway an indirect effect on the particles transport. The line emissions are calculated after the transport computation as $n_{\mathrm{im}}n_{\mathrm{e}}\mathrm{PEC}_{\lambda}(T_{\mathrm{e}})$, where $n_{\mathrm{im}}$ is the density of the impurity in the ionisation state of emission of the considered line and $\mathrm{PEC}_{\lambda}$ is the photon emission coefficient for the line $\lambda$ [28]. The perpendicular anomalous diffusion coefficient $D_{\perp}^{\mathrm{an}}$ was set, except where it will be explicitly differently reported, to be the value estimated for WEST in former works equal to 0.3 $\mathrm{m}^2/\mathrm{s}$ [18]. Outside the sheath, the electric field $\vec{E}$ was considered to be null.

# 4 Role of the different plasma-facing components in tungsten contamination

The heavy impurities contamination of the main plasma cannot be straightforwardly related to heavy impurity sources. In fact, even if the lower divertor is the PFC experiencing the highest incident particle and energy flux, the plasma particle flux itself screens wall impurities through friction. on the other hand, PFCs receiving a smaller incident particle flux could be the source for impurities that more likely end up crossing the separatrix and entering the confined plasma [29].
For this reason, it is important to test the contamination related to different PFCs, analyzing one component at a time in the simulations. This was done performing different ERO2.0 runs using only one PFC at a time as W source. This approach is reasonable only assuming that self-sputtering of a PFC caused by W originating from all other PFCs can be neglected. However, this working assumption was considered to be acceptable since, due

to the W strong screening, W particles are likely to re-deposit on the same PFCs from which they are sputtered.
The 6 PFCs for which this study was performed are antenna-limiter, inner wall, upper divertor, ceiling, baffle, and lower divertor. The latter was divided into its inner target and its outer target. Figure 4a shows the position in the poloidal section of these PFCs. Tables 1 and 2 show the peak values of the plasma parameters at the different PFCs in the two background plasma.

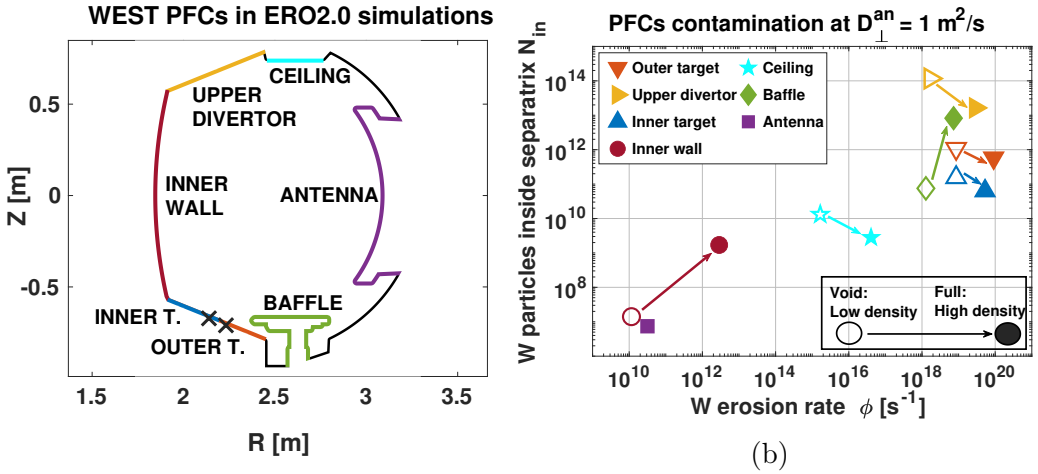


(a) (b)

Figure 4: a) WEST PFCs modelled in ERO2.0 as W source. Black crosses indicate the strike points. b) Core contamination $N_{\text{in}}$ as a function of W erosion rate $\phi_{\text{W}}$ for each PFC in low and high density plasma case, with $D_{\perp}^{\text{an}} = 1$ m$^2$/s.

| PFC peak value | $n_{\text{e}}$ [m$^{-3}$] | $T_{\text{e}}$ [eV] | $T_{\text{i}}$ [eV] | $v_{\parallel}$ [ms$^{-1}$] |
|---|---|---|---|---|
| Inner target | $2.3 \times 10^{19}$ | 16.2 | 16.6 | $3.5 \times 10^{4}$ |
| Outer target | $8.4 \times 10^{18}$ | 26.9 | 19.9 | $4 \times 10^{4}$ |
| Upper divertor | $5.2 \times 10^{18}$ | 19.2 | 20.2 | $3.2 \times 10^{4}$ |
| Inner wall | $1.2 \times 10^{15}$ | 0.9 | 6.7 | $1.2 \times 10^{4}$ |
| Ceiling | $2.2 \times 10^{17}$ | 6.0 | 10.0 | $2.1 \times 10^{4}$ |
| Antenna | $2.0 \times 10^{15}$ | 1.0 | 3.9 | $1.0 \times 10^{4}$ |
| Baffle | $2.5 \times 10^{18}$ | 11.5 | 15.0 | $1.2 \times 10^{4}$ |

Table 1: Low density background plasma properties peak values at the different PFCs.

| PFC peak value | $n_e$ [$m^{-3}$] | $T_e$ [eV] | $T_i$ [eV] | $v_{\parallel}$ [$ms^{-1}$] |
|---|---|---|---|---|
| Inner target | $1.1 \times 10^{20}$ | 23.6 | 20.0 | $3.1 \times 10^4$ |
| Outer target | $8.2 \times 10^{19}$ | 29.2 | 22.0 | $3.4 \times 10^4$ |
| Upper divertor | $8.2 \times 10^{19}$ | 24.5 | 25.5 | $3.4 \times 10^4$ |
| Inner wall | $2.7 \times 10^{15}$ | 1.1 | 9.3 | $1.7 \times 10^4$ |
| Ceiling | $5.9 \times 10^{17}$ | 7.7 | 13.1 | $2.1 \times 10^4$ |
| Antenna | $3.8 \times 10^{15}$ | 1.4 | 5.1 | $1.1 \times 10^4$ |
| Baffle | $1.2 \times 10^{19}$ | 10.7 | 17.6 | $1.6 \times 10^4$ |

Table 2: High density background plasma properties peak values at the different PFCs.

Figure 4b shows the total number of W particles found inside the separatrix in the simulations $N_{in}$ as a function of the W erosion rate $\phi_W$ (expressed in $s^{-1}$) for each considered PFC in both low and high density plasma cases using $D_{\perp}^{an} = 1\ m^2/s$. In the low density case, $T_i$ and $T_e$ at the antenna were too low for compute sputtering to occur, since the interpolated SDTrimSP5.0 results for O impacting W present a sputtering threshold at $E_i = 20$ eV. Therefore, no results are given for that PFC. On the other hand, for the high density case it was possible to study all the PFCs. It is possible to see how, passing from low density to high density conditions, $\phi_W$ increases but in most of the cases $N_{in}$ decreases, as simpler models would forecast [30], and also in accordance with former SolEdge-EIRENE + ERO2.0 modelling on WEST geometry [31].
This is not true for the baffle, as discussed further below in this section. Figure 4 also shows how, despite having a weaker source, the main chamber PFCs do not have a negligible contribution to the confined plasma contamination. However, there is strong uncertainty about the W source of some of the main chamber PFCs: the plasma flux at the upper divertor, and so the W erosion at this component, could be affected by uncertainties on the position of the secondary X-point in the magnetic equilibrium reconstruction. On the other hand, it should be remarked that the axisymmetric antenna modelled in the simulations is not as close to the separatrix as the actual, toroidally discrete, WEST antennae were during the experiment (see 1b, grey line). Therefore, $T_i$ and $T_i$ at this PFC are underestimated, and so is the sputtering yield (which is a very strong non-linear function of the $T_i$ and $T_i$).
The PFCs screening was assessed performing a study of the so-called W penetration factor $\tau_W$ [32, 33] defined in equation 1:

$$\tau_{\mathrm{W}} = \frac{N_{\mathrm{in}}}{\phi_{\mathrm{W}}} \tag{1}$$

$\tau_{\mathrm{W}}$ can be simply derived as follow: consider a single point model of the core W content. The balance of W particles inside it is given by equation 2:

$$\frac{dN_{\mathrm{in}}}{dt} = -\frac{N_{\mathrm{in}}}{\tau_{\mathrm{W}}^{\mathrm{c}}} + \alpha\phi_{\mathrm{W}} \tag{2}$$

Where $N_{\mathrm{in}}$ is the number of W particles inside the core, $\tau_{\mathrm{W}}^{\mathrm{c}}$ is the confinment time of W particles and $\alpha$ is a screening factor that takes into account all the redeposition phenomena that could cause eroded W particles to impact the wall before entering the core. It is straightforward that, if the initial core W content is zero, in the final steady state the core W content is given by equation 3:

$$N_{\mathrm{in}} = \alpha\phi_{\mathrm{W}}\tau_{\mathrm{W}}^{\mathrm{c}} = \phi_{\mathrm{W}}\tau_{\mathrm{W}} \tag{3}$$

In which we find again the $\tau_{\mathrm{W}}$ defition presented in equation 1. It has to be remarked that, since $\alpha$ is tipically very small for W, $\tau_{\mathrm{W}}$ can be several order of magnitude smaller than the physical time scales describing W confinment inside the core. The meaning of $\tau_{\mathrm{W}}$ is related to the probability of a particle, starting from a certain PFC, to enter the confined plasma. This gives an estimation of how much a PFC is screened, despite the source strength or the related uncertainty in the model. Moreover, computing $\tau_{\mathrm{W}}$ for different values of $D_{\perp}^{\mathrm{an}}$ allows one to assess the importance between this free parameter of the model on W contamination.

$D_{\perp}^{\mathrm{an}}$ is the simulation input parameter most affected by uncertainty but also one of the most relevant for what concerns W transport, so it is essential to perform a scan. The considered values of $D_{\perp}^{\mathrm{an}}$ are 0.3 and 1 $\mathrm{m}^2/\mathrm{s}$, values in the typical diffusion range in plasma SOL [24], also found to be consistent with WEST experiments [18, 21, 34], and the higher values 3 and 10 $\mathrm{m}^2/\mathrm{s}$ to model very high diffusion conditions.

The results (tab. 3 and tab. 4) show that, despite a much stronger source, the divertor PFCs (namely lower divertor targets and baffle) present a smaller value of $\tau_{\mathrm{W}}$ compared to the main chamber PFCs one, even at the highest considered value of $D_{\perp}^{\mathrm{an}}$ .

The small $\tau_{\mathrm{W}}$ values at the divertor can be explained both by its position and by the strong plasma flow that acts as a screen for impurities. On the other hand, the antenna and the inner wall have the highest $\tau_{\mathrm{W}}$ as their position causes particles to reach easily the separatrix. Moreover, at midplane the particle flux is 5 orders of magnitude lower than the one at the outer target. A non-axisymmetric antenna would have a different $\tau_{\mathrm{W}}$ that could

be even higher, if positioned closer and the separatrix, while the forecast of the overall source of all the antennae combined would be complicated without a 3D numerical model (less eroded surface, but higher $T_\mathrm{i}$ and $T_\mathrm{e}$, and higher plasma recycling that enhances $n_\mathrm{e}$). Also the effects of a more complex transport model (including e.g. an explicit term for thermal forces, a not null electric field $\vec{E}$ outside the sheath, non-uniform $D_\perp^\mathrm{an}$ distribution) are interesting opportunities for future developments.

| $\log_{10}(\tau_\mathrm{W}[\mathrm{s}])$ | $D_\perp^\mathrm{an} = 0.3$ m$^2$/s | 1 m$^2$/s | 3 m$^2$/s | 10 m$^2$/s |
|---|---|---|---|---|
| Inner wall | $-3.19$ | $-2.91$ | $-2.81$ | $-2.94$ |
| Upper divertor | $-4.07$ | $-4.16$ | $-4.24$ | $-4.43$ |
| Ceiling | $-7.07$ | $-5.10$ | $-4.05$ | $-3.80$ |
| Baffle | $< -12$ | $-7.23$ | $-5.43$ | $-5.17$ |
| Inner target | $-8.02$ | $-7.53$ | $-6.64$ | $-6.21$ |
| outer target | $< -12$ | $-6.90$ | $-6.54$ | $-5.63$ |

Table 3: $\log_{10}(\tau_\mathrm{W}[\mathrm{s}])$ in low density plasma case. Simulations were not statistically capable to detect very low values, these are expected to be $< -12$.

| $\log_{10}(\tau_\mathrm{W}[\mathrm{s}])$ | $D_\perp^\mathrm{an} = 0.3$ m$^2$/s | 1 m$^2$/s | 3 m$^2$/s | 10 m$^2$/s |
|---|---|---|---|---|
| Antenna | $-4.64$ | $-3.63$ | $-3.34$ | $-3.40$ |
| Inner wall | $-3.76$ | $-3.23$ | $-3.06$ | $-3.12$ |
| Upper divertor | $-6.46$ | $-6.24$ | $-5.92$ | $-5.64$ |
| Ceiling | $< -12$ | $-7.16$ | $-4.75$ | $-4.26$ |
| Baffle | $-8.54$ | $-5.95$ | $-5.70$ | $-5.80$ |
| Inner target | $-11.56$ | $-8.92$ | $-7.56$ | $-7.21$ |
| outer target | $-11.86$ | $-8.20$ | $-7.91$ | $-7.44$ |

Table 4: $\log_{10}(\tau_\mathrm{W}[\mathrm{s}])$ in high density plasma case. Simulations were not statistically capable to detect very slow values, these are expected to be $< -12$.

In the high density case, $\tau_\mathrm{W}$ is noticeably smaller for most of the PFCs. This is explained by the enhancement of prompt redeposition with $n_\mathrm{e}$ [35]. Exceptions to this behavior are represented by the inner wall and the baffle. For the former $\tau_\mathrm{W}$ values are slightly lower in the high density case, but they remain on the same order of magnitude. For the latter, at low $D_\perp^\mathrm{an}$ values, $\tau_\mathrm{W}$ becomes higher when $n_\mathrm{e}$ is higher. This is caused by the very

small perpendicular distance of this PFC to the separatrix, combined to the fact that high density slightly enhances perpendicular transport (while the parallel transport is weakened). The upper divertor and the ceiling $\tau_W$ are the ones that mostly decrease between the two cases. This is caused by the possible overestimation of plasma flux and screening at the top of the machine as described above (see section 2).
In the simulations, at low $D_\perp^{an}$ values the probability for W particles to reach the confined region is reduced by parallel transport and the friction with the plasma. These mechanisms flush W particles back towards the PFCs, causing them to redeposit before they can enter the confined plasma. In this regime, increasing $D_\perp^{an}$ helps particles entering the core, so $\tau_W$ increases with $D_\perp^{an}$. At high $D_\perp^{an}$ values, diffusion is strong enough to make most particles enter the core. A further increase of $D_\perp^{an}$ not only makes particles more easily enter the confined plasma, but also leave it. This is the reason why at high $D_\perp^{an}$ values $\tau_W$ reahces a plateau or even a small roll-over. Even if counterintuitive, the results obtained in the high diffusion cases are in qualitative agreement with analytical transport models for generical sputtered impurities described in litterature [24].

# 5 Role of light impurities content in tungsten contamination

If $\tau_W$ was independent of the conditions of the background plasma at the wall, it would be possible to linearly scale $N_{in}$ with the erosion rate using equation 1. However, the properties of the incident plasma flux at the wall influence heavy impurities transport in several ways. Since in L-mode the sputtering of heavy impurities is mostly caused by light impurities, it is worth studing the effect of O content on $\tau_W$. Here we use the outer lower divertor target as a proxy for all the PFCs since in the former study it had very low $\tau_W$, so it is supposed to be very sensitive to changes of input parameters that could enhance contamination. In this exercise, 3 different configurations of O content in the plasma were considered: 1% and 3% of O (with the same ions mixture described above in section 3) and finally 3% of only $O^{3+}$ content. This analysis was performed on the low density plasma background.
Results are shown in tab. 5: 1% O and 3% O concentration cases lead to equivalent $\tau_W$ (despite small fluctuations for low $D_\perp^{an}$ explicable by the effect of MC noise on very small $\tau_W$ values).

The cases with 3% $O^{3+}$ show values of $\tau_W$ up to 100 times higher then

| O.T. $\log_{10}(\tau_W[s])$ | $D_\perp^{an} = 0.3$ m$^2$/s | 1 m$^2$/s | 3 m$^2$/s | 10 m$^2$/s |
|---|---|---|---|---|
| 1%O | −9.97 | −8.50 | −6.43 | −5.58 |
| 3%O | −10.12 | −8.15 | −6.54 | −5.63 |
| 3%$O^{3+}$ | −8.05 | −7.00 | −6.28 | −5.42 |

Table 5: Outer target $\log_{10}(\tau_W[s])$ in low density plasma case under different plasma O contents. In the first two cases the mixture of O charge states described formerly in the paper was used (section 3), in the last one only $O^{3+}$ was considered.

the ones in the previous 2 cases. These $\tau_W$ values get closer to the previous two cases as $D_\perp^{an}$ increases. The reason is that $E_i$ depends on $Z$, therefore, higher charge of plasma components not only increases W erosion but also increases the initial energy that sputtered W atoms can reach. This, in turn, influences the impurities capability to avoid redeposition before crossing the separatrix (as it will be discussed in more detail in the next section). Similar considerations were pointed out in [36]. If $D_\perp^{an}$ is high, the difference in light impurities charge is not particularly relevant. When $D_\perp^{an}$ is equal or less than 1 m$^2$/s this effect has instead a strong impact on a very screened component as the outer divertor target. In [30] it is also possible to see how the fraction of non-redeposited W particles can change significantly if the energy of the sputtered W atoms increases. It has to be pointed out that between the first 2 cases and the last one $Z_{eff}$ changes by the 15%. This also have effects on the results, but they were not further investigated here.
In high diffusion conditions the initial energy of sputtered W neutrals becomes less relevant, but simulations with 3% $O^{3+}$ content show anyway $\tau_W$ values 1.5-2 times higher than the the two other cases.
This study shows how the charge of the light impurities influences W redeposition, moreover it is very well known how it also influences W erosion [24]. The combined result of these two effects is shown in figure 5 ($D_\perp^{an} = 3$ m$^2$/s in these simulations). The values of $\phi_W$, $\tau_W$, and $N_{in}$ for the two cases are shown in table 6.

Finally, it is interesting to study the prompt, the local, and the far redeposition in the two simulation shown in figure 5. These were evaluated calculating the distance from the W particles sputtering point and the point of their deposition at the wall $d$. Every particle deposited less than 1 cm away from the emission point was considered to be promptly redeposited. This threshold length was chosen since it should be equal to a few $W^{1+}$ Lar-

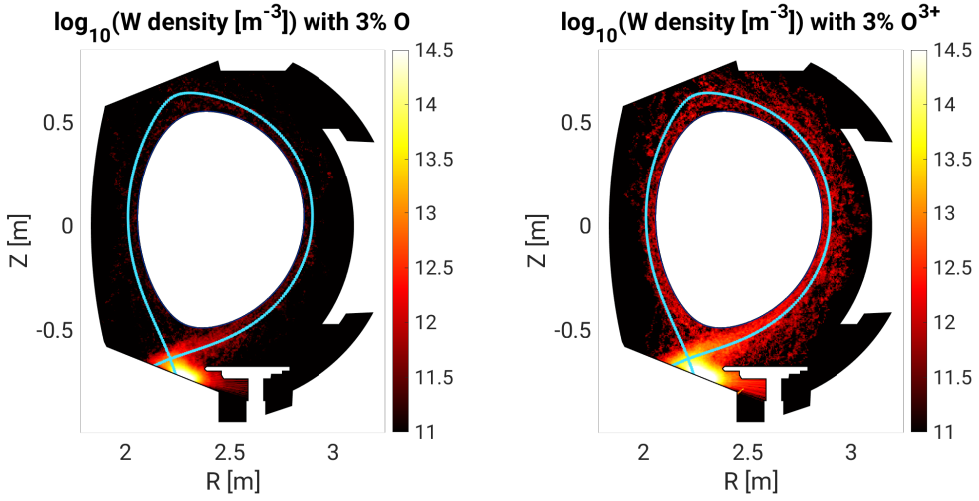


(a) (b)

Figure 5: W density poloidal map using only the outer target as W source and a background plasma (low density one) with 3% O concentration, in a) a mixture of the first 3 O ionisation states are used (see section 3), in b) only $O^{3+}$ is present in the background. $D_{\perp}^{\mathrm{an}} = 3\ \mathrm{m}^2/\mathrm{s}$ in the simulations.

| $D_{\perp}^{\mathrm{an}} = 3\ \mathrm{m}^2/\mathrm{s}$ | $\phi_{\mathrm{W}}$ $[10^{19}\ \mathrm{s}^{-1}]$ | $\tau_{\mathrm{W}}$ $[10^{-7}\ \mathrm{s}]$ | $N_{\mathrm{in}}$ $[10^{19}]$ |
|---|---|---|---|
| 3%O | 0.86 | 2.9 | 2.5 |
| 3%$O^{3+}$ | 3.03 | 5.2 | 15.9 |

Table 6: $\phi_{\mathrm{W}}$, $\tau_{\mathrm{W}}$, and $N_{\mathrm{in}}$ using only the outer target as W source, $D_{\perp}^{\mathrm{an}} = 3\ \mathrm{m}^2/\mathrm{s}$ ,and a background plasma (low density one) with 3% O concentration, using different O charge mixture.

mor radii that, at the background plasma condition at the outer target, shall corresponds to approximately 2 mm. Every particle deposited less than 1 m (but more than 1 cm) away from the target was considered to be locally redeposited, while for greater distances they were considered far redeposited. Results are presented in table 7.

The results show that increasing the background componets charge actually decreases the fraction of prompt redeposited particles. The ratio between local and far redeposition is similar in the two simulations, with a slightly more likely far redeposition when the background charge is higher. In the simulation with lower background charge, 12.5% of the non-promptly redeposited particles are far redeposited. With a higher background charge this fraction rises to 13%.

| Deposition type | Prompt ($d < 1$ cm) | Local ($d \leqslant 1$ m) | Far ($d > 1$ m) |
|---|---|---|---|
| 3%O | 92.0% | 7.0% | 1.0% |
| 3%$O^{3+}$ | 88.5% | 10.0% | 1.5% |

Table 7: Particles redeposition type fraction, based on the distance $d$ between the particles sputtering point and the point of their deposition at the wall. The simulations are the same described for figure 5.

# 6 Self-sputtering related contamination

Sputtering caused by W impurities impacting the wall is different from sputtering due to light species. First of all, a unitary mass ratio brings high energy transfer into a collision, and hence the sputtering yield increases rapidly with incident energy. Beyond a certain threshold ($\approx 270$ eV for an incidence angle of 60 °, according to the Eckstein fit formula [37]) the cascade effect created by W impacting the wall is so strong that it's possible that even more than one W atom can be sputtered for each W ion impacting the wall, so the sputtering yield rises above 1. Also, incident energy of W impacting wall can be higher than the one carried by a light species: W ions can easily deposit with an ionisation state higher than 1 and this brings a high acceleration in the plasma sheath. Moreover, near the divertor targets, plasma friction can push W ions to a speed equal to a fraction of the plasma sound-speed ($c_s$), and since $\frac{m_W}{m_D} = 92$ these ions have very large kinetic energy. Finally, during W self-sputtering, the cut-off of the initial W sputtered neutrals energy distribution has usually higher values than during sputtering by light impurities [38]. In fact, considering e.g. a projectile incident energy of 200 eV the cut-off energy value for W sputtering by O is 33 eV, while for W self-sputtering is 130 eV. Similar considerations have been extensively discussed in literature [39, 40].
In this work self-sputtering was examined over the two different backgrounds plasma, the simulations were iterated until reaching a convergence of the wall erosion rate, with each ERO2.0 iteration reading self-sputtering of W particles deposited in the previous step. O concentration was set according to the way described in section 3.

Background plasma sputtering and self-sputtering at the two divertors in the low density plasma background case are shown in figure 6a. The self-sputtering contribution is not pronunced at lower divertor targets (10-20% of intensification of the gross W flux), while a more significant erosion enhancement can be seen the at the upper divertor (60% of intensification

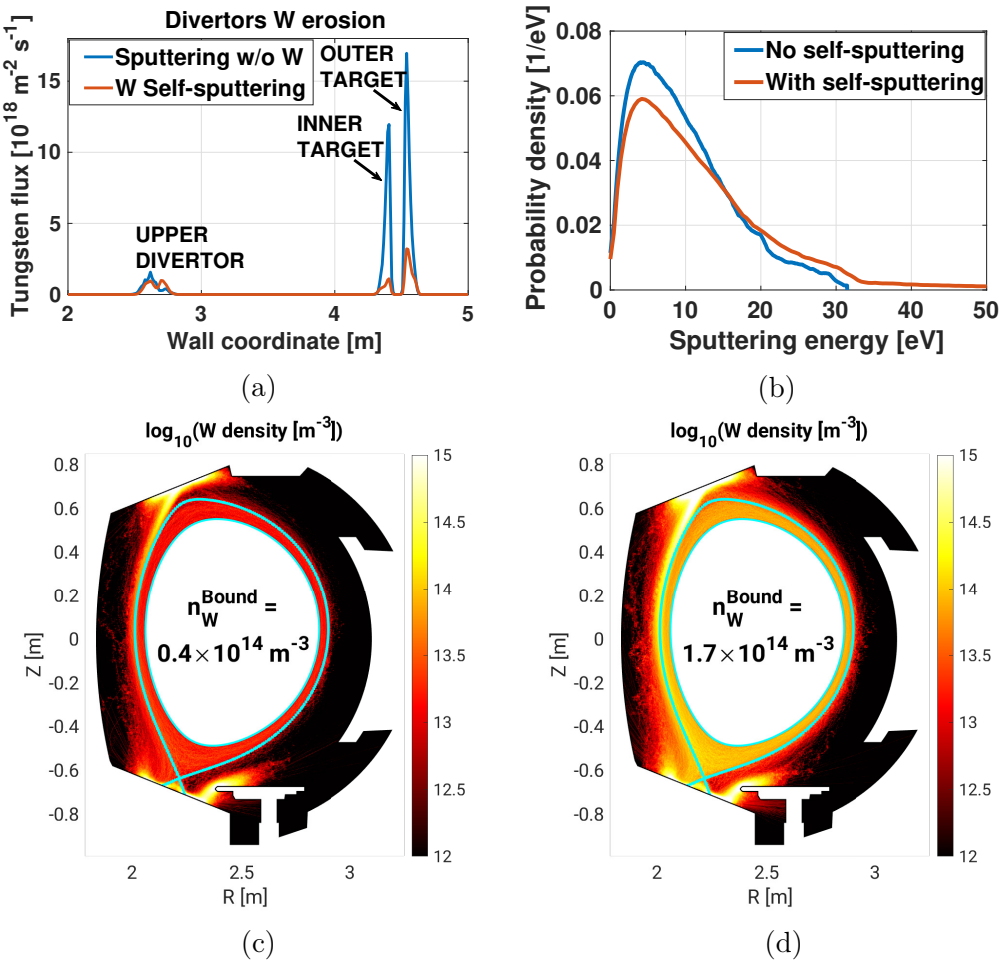


Figure 6: a) Plasma background sputtering and W self-sputtering at the two divertors in low density plasma background case. b) Test particles sputtering energy probability density in low density plasma background in steady-state without and with self-sputtering. c) Poloidal W density map without self-sputtering, and d) with self-sputtering. O concentration was set according to the description of section 3.

of the gross W flux). However, there is only a factor of 1.3 between total wall erosion rate in the cases with and without self-sputtering. A significant difference in the sputtering energy of the particles (i.e. the initial energy of sputtered W a) is observed (6b): 31 eV is the maximum sputtering energy achieved in the simulation without self-sputtering. In the simulation with self-sputtering, 10% of the particles reach sputtering energies from 30 eV to beyond 100 eV.

The higher sputtering energy is explained by the high deposition energy of

projectile W particles impacting the wall. These heavy impurities can impact the wall at higher energy than the light ones present in the background plasma, as explained above at the beginning of the section.

The effect of the high sputtering energy of part of the particles can be seen in figure 6c and 6d. In this figure two different poloidal maps of $n_{\mathrm{W}}$ are shown for the simulations corresponding to the cases without and with self-sputtering. Inside the inner boundary it is possible to read the average W density at the inner-boundary surface $n_{\mathrm{W}}^{\mathrm{Bound}}$. The average W density on the inner-boundary increases by a factor $\approx 4-5$ between the case with and without self-sputtering so, even if the wall erosion rate has only increased by a factor of 1.3, the density at the inner boundary noticeably increased.

This result can be explained as follows: taking as an example the lower divertor, the most important redeposition mechanism is the redeposition during the first Larmor gyration (prompt redeposition). However, this mechanism is not influenced at all by particles sputtering energy, as it depends on the ratio between W neutrals ionisation length and $\mathrm{W}^{1+}$ Larmor radius, and so it is indipendent by W speed [30]. The rest of the main redeposition mechanisms are related to the electric field present in the plasma sheath $\vec{E}_{\mathrm{sheath}}$ and the friction with the plasma flowing to the target with a speed that, for the Bohm criterion, increases up to the sound speed at the sheath entrance. If W ions have high enough energy, they can exit the region of strong forces pushing them towards the targets. Otherwise, they will be decelerated until their trajectory is reversed and they will return to the targets (with energy being generally lower than the one they would have exiting the high redeposition region and then re-entering it). This explanation is similar to the one given in [30], in which only the effect of $\vec{E}_{\mathrm{sheath}}$ was considered, while the effects of the background plasma friction were only qualitatively discussed, but not included in the simulations.
The results for the high density plasma background case are quite different: the total wall erosion rate increases between the cases without and with self-sputtering only by 1.5%. The difference of particles impact energy between the two different plasma background cases for the simulations without self-sputtering is shown in figure 7c: W particles in the low density case have higher average impact energy than in the high density case (112 eV the first, 32 eV the latter). The reason is the enhancement of promptly redeposition under high density conditions. Promptly redeposited W ions impact the wall with an energy similar to the one they had as atoms after being sputtered, while particles that are not promptly re-deposited can gain energy from the plasma with the mechanisms discribed above. Moreover, since the

self-sputtering yield is a very non-linear function of the $E_{\mathrm{i}}$, the difference of impact energy is translated into a huge difference in self-sputtering yield between the low and high density case: on average it is equal to $5.55 \times 10^{-4}$ in high density case, and $1.85 \times 10^{-1}$ in low density case.

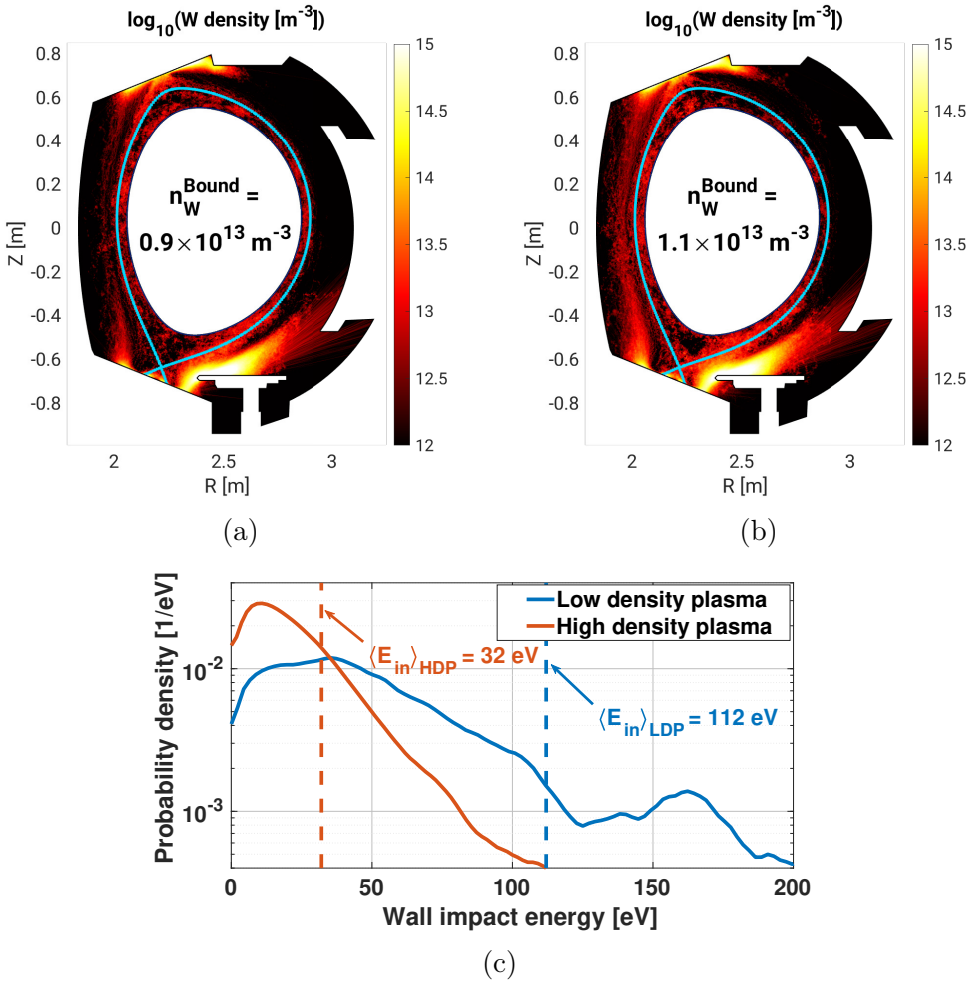


Figure 7: Poloidal W density map in high density plasma case a) without self-sputtering, and b) with self-sputtering. c) W wall impact energy in low and high density plasma case (self-sputtered impurities not included). Dashed lines show the average impact energy for the low density plasma (LDP) case and high density plasma (HDP) case. O concentration was set according to the description of section 3.

This can be explained by the important role of $n_{\mathrm{e}}$ in W redeposition: both ionisation rate and plasma friction scale linearly with density, and these

phenomena strongly influence redeposition. The effect of the higher $T_e$ in the high density case is not straightforward: higher $T_e$ means higher sputtering energy (or self-sputtering energy, i.e. the sputtering energy of self-sputtered W particles), but also stronger sheath potential, ionisation rate, and friction force (through $c_s$). However, this study did not focus on such aspects and here we just state that in the high density case increasing $T_e$ did not correspond to a reduction of redeposition.
Figure 7a and 7b show poloidal $n_W$ maps in the simulations without and with self-sputtering performed for the high density plasma case background, density at the separatrix is lower then in the previous case. Self-sputtering does not cause relevant changes on $n_W^{Bound}$. In this case, $n_W^{Bound}$ goes from $0.9 \times 10^{13}$ m$^{-3}$ without self-sputtering to $1.1 \times 10^{13}$ m$^{-3}$ with self-sputtering. This is way less relevant then the effect of self-sputtering in the low density case, in which $n_W^{Bound}$ goes from $0.4 \times 10^{14}$ m$^{-3}$ without self sputtering to $1.7 \times 10^{14}$ m$^{-3}$ with self-sputtering.

These considerations explain how self-sputtering can be both a very important mechanism of contamination and a very difficult phenomenon to forecast. However, simulations show that increasing density could be the way to control this contamination threat in L-mode discharges. These conclusion are similar to ones made in [30] about W self-sputtering in H-mode discharges.
The complexity of the problem highlights the need of having some comparison with experiments. The lower divertor source is probably the more appropriate quantity to compare with experiments, since it is both the stronger one and the one that receives usually more attention by experimental measaurements. Indeed, also signals are higher and measurements easier to deal with.

# 7 Lower divertor tungsten source: model to experiment comparison

In order to compare the simulated lower divertor W source to the experimental one, synthetic diagnostics were used to reproduce visible spectroscopy. The synthetic diagnostics consist of post-processing the 2D emission map of a given visible wavelength of W calculated by ERO2.0 using SYNDI (a MC beam tracer) [21], so that it is possible to obtain the line-integrated photon flux on the WEST visible spectroscopy system lines of sight. This allows for a direct one-to-one comparison between experiments and SolEdge-EIRENE + ERO2.0 simulations. Alternatively, an experimentally estimated inverse photon efficiency could have been used to estimate the W photon flux from

the particle flux [41]. Figure 8 shows the lines of sight considered by simulations and the ones available in the experiment.

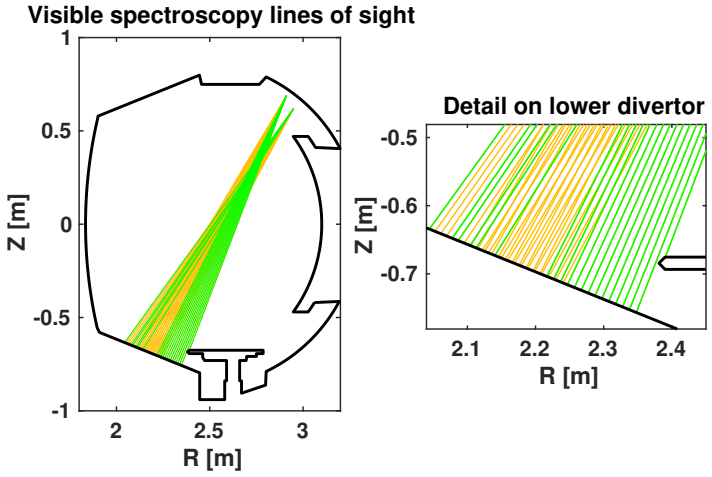


Figure 8: Visible spectroscopy lines of sight pointing at the lower divertor. Yellow lines were only modelled in simulations, while green ones were both reproduced in simulations and available in the experiment.

The wavelength for which the visible spectroscopy data were analysed is the standard WI line 400.9 nm. The two targets were simulated separately since this allows to assume different O concentration for each target, so the small effect of photons emitted from the other target was neglected. The self-sputtering was also neglected as it does not influence much erosion, as previously discussed. Since erosion depends on O content, the experimental O visible signal OII 435.1 nm at the targets (figure 9) was used to make an educated guess on the O concentration ratio to set in the simulations. During the first time interval (3-3.5 s) the OII signal is strongly unbalanced between the targets, with a difference of about one order of magnitude. Then, in the second time interval (5-.5 s), the signal peaks at the targets become very similar. It is not clear how much the unbalanced configuration depends on $n_e$ and $T_e$ difference between the targets and how much it depends on an actual O concentration difference. However, light impurities self-consistent numerical modelling in former works have shown that it is possible to have O concentration unbalances between the WEST divertor targets with a slightly higher O content at the inner target [21].

An O concentration scan was performed in ERO2.0 for each target in each plasma density case. In the low density case the O concentration values set for the simulations were 1%, 2%, and 3% for the inner target , 0.1%,

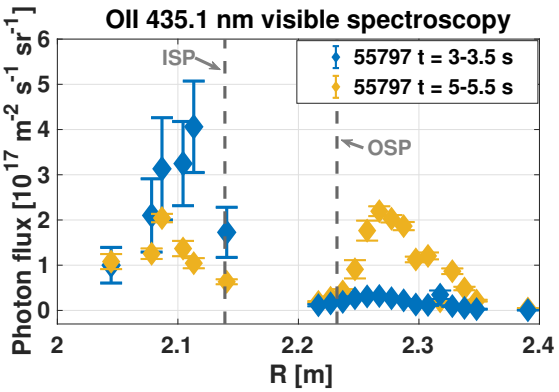


Figure 9: Visible signal of OII 435.1 nm line during the two considered time intervals.

0.2%, and 0.3% for the outer target, while in the high density plasma the values 0.1%, 0.2%, and 0.3% were used for both the targets. Results are shown in figure 10: in the low density case the WI photon flux profile was very well reproduced at the outer target for O concentration equal 0.2% , while for the inner target a value of 3% was needed. This difference in the W visible signal between the targets is qualitatively similar to the one seen in the experiment for the OII line during the interval $3 - 3.5$ s. During the interval $5 - 5.5$ s, the WI 400.9 nm signal recovers some symmetry. In high density plasma simulations a good agreement at the outer target is found for O concentration equal to 0.1% with the shape again well reproduced, while for the inner target the shape is not recovered even when the magnitude of the peak is similar, with the peak itself being also shifted in position.

Very good agreement was obtained for the time interval $t = 3 - 3.5$ s on both targets, and for the the time interval $t = 5 - 5.5$ s on the outer target. On the inner target during the time interval $t = 5 - 5.5$ s, the observed mismatch in the profile could be improved in future efforts by implementing spatially resolved light impurity profiles in the code. Nevertheless, it is possible to obtain comparable results tuning O concentration on physically acceptable values, this can be useful to reduce the uncertainty related to the lower divertor source and move the analyses to the study of other PFCs.

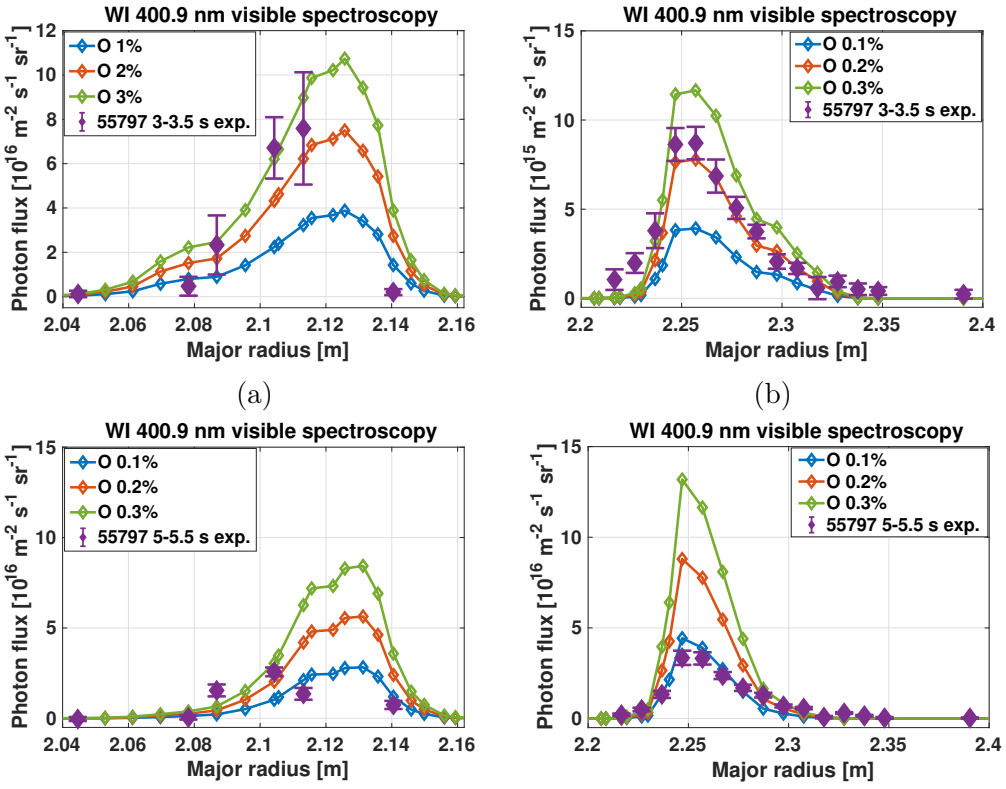


Figure 10: visible synthetic diagnostics signal and comparison with WI 400.9 nm experimental data at inner and outer targets in low density plasma case (a and b respectively), and inner and outer targets in high density plasma case (c and d respectively). Notice that the signal order of magnitude in (b) is smaller than in the other plots.

# 8 Conclusions

W contamination in WEST was studied through ERO2.0 numerical modelling starting from SolEdge-EIRENE simulations of the background plasma of two different phases of the WEST discharge #55797. The contamination contribution from different PFCs was investigated, suggesting that PFCs experiencing a smaller incident particle flux can can have an important role in contamination. In accordance with former publications [30, 31], simulations showed that passing from a low to a high density background plasma, W sources increases but the confined plasma contamination weakens for most of the PFCs.

To overcome the model uncertainties concerning W sources, the penetration

factor $\tau_W$ was computed for each PFC for both background plasma density case assuming different anomalous diffusion coneffiecients. This study showed that the lower divertor is the best screened PFC in most conditions, while the main chamber PFCs are usually very weakly screened. Besides this, the upper divertor and the antenna-limiter need a closer investigation since they are suspected to have an important role in WEST W contamination but also to be subject to strong uncertainties in the model, while the baffle screening is the most sensitive to the plasma and diffusion conditions.
The influence of light impurities plasma content in W contamination was studied through $\tau_W$ using different O concentrations and charge mixtures in the simulations, which showed that not only W sources are influenced by light impurities charge, but also the probability of sputtered W particles to enter into the confined plasma avoiding redeposition mechanisms.
Self-sputtering was also modelled. Results were very different in the two plasma density cases: in the low density case W impurities impacting the wall cause a slight erosion enhancement due to self-sputtering. Nevertheless, their impact speed was high enough to allow self-sputtered impurities to have sufficient energy to escape redeposition mechanisms and heavily increase confined plasma contamination. In the high density case the high prompt redeposition does not allow W impurities to gain much energy from the plasma, so their impact speed is not high enough to influence either erosion or confined plasma contamination through self-sputtering.
Finally, a direct comparison with the WI 400.9 nm visible signal measured at the divertor targets was performed using a synthetic diagnostic. The OII 435.1 nm line signal trend in the discharge was used as an indication for the simulations O concentration ratio between the targets in the two modelled plasma discharge phases. The results showed a good agreement with the experimental data for values of O concentration between 0.1% and 3%, and the capability of the model to reproduce a realistic W visible signal shape at the outer target.
In the future the model could be improved by different aspects: with the future development of 3D plasma transport code working in realistic geometry, the passage to 3D background plasma with a complex wall and magnetic ripples could be an important step ahead for the modelling of W sources from toroidally discrete objects like WEST antennas and limiters.. A self-consistency in light impurities sputtering could improve the source and sputtering energy estimation. Finally, comparison with main chamber sources would help the accuracy of the source estimation for weakly screened PFCs.

# Acknowledgement

This work has been carried out within the framework of the EUROfusion Consortium and has received funding from the Euratom research and training programme 2014-2018 and 2019-2020 under grant agreement No 633053. The views and opinions expressed herein do not necessarily reflect those of the European Commission.


# References


[1] R. A. Pitts et al. Physics conclusions in support of ITER W divertor monoblock shaping. *Nuclear Materials and Energy*, 12:60–74, 2017. *Proceedings of the 22nd International Conference on Plasma Surface Interactions 2016, 22nd PSI.*

[2] J. Bucalossi et al. The WEST project: Testing ITER divertor high heat flux component technology in a steady state tokamak environment. *Fusion Engineering and Design*, 89(7):907–912, 2014. *Proceedings of the 11th International Symposium on Fusion Nuclear Technology-11 (ISFNT-11) Barcelona, Spain, 15-20 September, 2013.*

[3] O. Meyer et al. Visible spectroscopy diagnostics for tungsten source assessment in the WEST tokamak: first measurements. *Review of Scientific Instruments*, 89(10):10D105, 2018.

[4] G. J. van Rooij et al. Tungsten divertor sources in WEST related to impurity inventory and local plasma conditions. *Physica Scripta*, T171:014060, jan 2020.

[5] H. Bufferand et al. Numerical modelling for divertor design of the WEST device with a focus on plasma–wall interactions. *Nuclear Fusion*, 55(5):053025, apr 2015.

[6] J. Romazanov et al. Beryllium global erosion and deposition at JET-ILW simulated with ERO2.0. *Nuclear Materials and Energy*, 18:331–338, 2019.

[7] J. Romazanov et al. First monte-carlo modelling of global beryllium migration in ITER using ERO2.0. *Contributions to Plasma Physics*, 60(5-6):e201900149, 2020.

[8] S. Dai et al. EMC3-EIRENE modelling of edge impurity transport in the stochastic layer of the large helical device compared with extreme ultraviolet emission measurements. *Nuclear Fusion*, 56(6):066005, 2016.

[9] S. Yamoto et al. Kinetic modeling of high-Z tungsten impurity transport in ITER plasmas using the IMPGYRO code in the trace impurity limit. *Nuclear Fusion*, 57(11):116051, aug 2017.

[10] S. Brezinsek et al. Erosion, screening, and migration of tungsten in the JET divertor. *Nuclear Fusion*, 59(9):096035, aug 2019.

[11] B. Faugeras. An overview of the numerical methods for tokamak plasma equilibrium computation implemented in the NICE code. *Fusion Engineering and Design*, 160:112020, 2020.

[12] D. Reiter et al. The EIRENE and B2-EIRENE codes. *Fusion Science and Technology*, 47(2):172–186, 2005.

[13] H. Bufferand et al. Three-dimensional modelling of edge multi-component plasma taking into account realistic wall geometry. *Nuclear Materials and Energy*, 18:82–86, 2019.

[14] H. Bufferand et al. Progress in edge plasma turbulence modelling hierarchy of models from 2D transport application to 3D fluid simulations in realistic tokamak geometry. *Submitted to Nuclear Fusion*, 2021.

[15] H. Bufferand et al. Description of the model Application to 2D transport modelling Application to 3D turbulence modelling. Presented at: *Third IAEA Technical Meeting on Divertor Concepts, Vienna, November 2019*.

[16] J.P. Gunn et al. Evidence for a poloidally localized enhancement of radial transport in the scrape-off layer of the Tore Supra tokamak. *Journal of Nuclear Materials*, 363-365:484–490, 2007. Plasma-Surface Interactions-17.

[17] R. Dejarnac et al. Flush-mounted langmuir probes in the WEST tokamak divertor. *Fusion Engineering and Design*, 163:112120, 2021.

[18] G. Ciraolo et al. Impact of divertor configuration on tokamak performances: focus on WEST experiments supported by SOLEDGE2D modeling. Presented at: *Third IAEA Technical Meeting on Divertor Concepts, Vienna, November 2019*.

[19] C. Gil et al. Renewal of the interfero-polarimeter diagnostic for WEST. *Fusion Engineering and Design*, 140:81–91, 2019.

[20] F. Clairet et al. Fast sweeping reflectometry upgrade on Tore Supra. *Review of Scientific Instruments*, 81(10):10D903, 2010.

[21] A. Gallo et al. Interpretative transport modeling of the WEST boundary plasma: main plasma and light impurities. *Nuclear Fusion*, 60(12):126048, nov 2020.

[22] J. Romazanov et al. First ERO2.0 modeling of be erosion and non-local transport in JET ITER-like wall. *Physica Scripta*, T170:014018, sep 2017.

[23] D. Tskhakaya. One-dimensional plasma sheath model in front of the divertor plates. *Plasma Physics and Controlled Fusion*, 59(11):114001, sep 2017.

[24] P.C. Stangeby. *The Plasma Boundary of Magnetic Fusion Devices*. Series in Plasma Physics and Fluid Dynamics. Taylor & Francis, 2000.

[25] A. Eksaeva et al. ERO modelling of tungsten erosion in the linear plasma device PSI-2. *Nuclear Materials and Energy*, 12, 03 2017.

[26] A. Eksaeva et al. Surface roughness effect on Mo physical sputtering and re-deposition in the linear plasma device PSI-2 predicted by ERO2.0. *Nuclear Materials and Energy*, 19:13–18, 2019.

[27] A. Mutzke et al. Ion fluence dependence of the si sputtering yield by noble gas ion bombardment. *Nuclear Instruments and Methods in Physics Research Section B: Beam Interactions with Materials and Atoms*, 266(6):872 – 876, 2008.

[28] H. P. Summers. The ADAS user manual. 2004.

[29] A. Sepetys. *Tungsten sources in the divertor and the main chamber and contamination of the WEST tokamak plasmas*. Theses, Aix Marseille Universitè ; cea cadarache, December 2019.

[30] A. V. Chankin et al. Monte carlo simulations of tungsten redeposition at the divertor target. *Plasma Physics and Controlled Fusion*, 56(2):025003, jan 2014.

[31] A. Gallo et al. First efforts in numerical modeling of tungsten migration in WEST with SolEdge2D-EIRENE and ERO2.0. *Physica Scripta*, T171:014013, 2020.

[32] N. Fedorczak et al. Tungsten transport and sources control in JET ITER-like wall H-mode plasmas. *Journal of Nuclear Materials*, 463, 12 2014.

[33] R. Dux et al. Main chamber sources and edge transport of tungsten in H-mode plasmas at ASDEX upgrade. *Nuclear Fusion*, 51(5):053002, apr 2011.

[34] G. Ciraolo et al. First modeling of strongly radiating WEST plasmas with SOLEDGE-EIRENE. *Nuclear Materials and Energy*, 20:100685, 2019.

[35] A. Kirschner et al. Modelling of plasma-wall interaction and impurity transport in fusion devices and prompt deposition of tungsten as application. *Plasma Physics and Controlled Fusion*, 60(1):014041, nov 2017.

[36] Y. Marandet et al. Assessment of tungsten sources in the edge plasma of WEST. *Journal of Nuclear Materials*, 463:629–633, 2015. PLASMA-SURFACE INTERACTIONS 21.

[37] W. Eckstein R. Behrisch. *Sputtering by Particle Bombardment.* Topics in Applied Physics. Springer-Verlag Berlin Heidelberg, 2007.

[38] A. Kirschner. Erosion and Deposition mechanisms in Fusion Plasmas. *Fusion Science and Technology*, 61(2T):230–245, 2012.

[39] J. N. Brooks. Modeling of sputtering erosion/redeposition status and implications for fusion design. *Fusion Engineering and Design*, 60(4):515–526, 2002.

[40] D. Naujoks et al. Erosion and redeposition in the ASDEX upgrade divertor. *Journal of Nuclear Materials*, 210(1):43–50, 1994.

[41] S. Brezinsek et al. Spectroscopic determination of inverse photon efficiencies of W atoms in the scrape-off layer of TEXTOR. *Physica Scripta*, T170:014052, oct 2017.